Int J CARS
DOI 10.1007/s11548-017-1603-8

ORIGINAL ARTICLE

# BEM-based simulation of lung respiratory deformation for CT-guided biopsy

**Dong Chen**[1] · **Weisheng Chen**[2] · **Lipeng Huang**[2] · **Xuegang Feng**[2] ·
**Terry Peters**[3] · **Lixu Gu**[1]

Received: 10 October 2016 / Accepted: 27 April 2017

**Abstract**

*Purpose* Accurate and real-time prediction of the lung and lung tumor deformation during respiration are important considerations when performing a peripheral biopsy procedure. However, most existing work focused on offline whole lung simulation using 4D image data, which is not applicable in real-time image-guided biopsy with limited image resources. In this paper, we propose a patient-specific biomechanical model based on the boundary element method (BEM) computed from CT images to estimate the respiration motion of local target lesion region, vessel tree and lung surface for the real-time biopsy guidance.

*Methods* This approach applies pre-computation of various BEM parameters to facilitate the requirement for real-time lung motion simulation. The resulting boundary condition at end inspiratory phase is obtained using a nonparametric discrete registration with convex optimization, and the simulation of the internal tissue is achieved by applying a tetrahedron-based interpolation method depend on expert-determined feature points on the vessel tree model. A reference needle is tracked to update the simulated lung motion during biopsy guidance.

*Results* We evaluate the model by applying it for respiratory motion estimations of ten patients. The average symmetric surface distance (ASSD) and the mean target registration error (TRE) are employed to evaluate the proposed model. Results reveal that it is possible to predict the lung motion with ASSD of $1.9 \pm 0.8$ mm and a mean TRE of $2.5 \pm 2.1$ mm at largest over the entire respiratory cycle. In the CT-/electromagnetic-guided biopsy experiment, the whole process was assisted by our BEM model and final puncture errors in two studies were 3.1 and 2.0 mm, respectively.

*Conclusion* The experiment results reveal that both the accuracy of simulation and real-time performance meet the demands of clinical biopsy guidance.

**Keywords** Biopsy · Biomechanical model · Lung motion prediction · Boundary element method

## Introduction

Lung cancer leads cancer-related mortality in the world and kills over 150,000 people each year in the USA alone [1]. Early and accurate diagnosis is the key for the optimal treatment of lung cancer patients. Lung biopsy removes a small piece of lung tissue that can be studied histologically to detect the presence of disease. While respiratory motion introduces uncertainties in the location of target tissue, accurate and real-time tracking position of lung tumors and probes during respiratory motion is a serious challenge of clinical biopsy guidance.

The three common types of lung biopsy employ open, bronchoscopic or percutaneous approaches. Open biopsy is a minimally invasive procedure where the surgeon opens the suspected area to extract the biopsy sample. This approach is usually performed when the other methods of lung biopsy have been unsuccessful. Bronchoscopic biopsy uses a bronchoscope inserted through the mouth or nose and into the airway to collect a lung tissue sample. However, current bronchoscopes cannot access the majority of the peripheral lung,

✉ Lixu Gu
gulixu@sjtu.edu.cn

[1] School of Biomedical Engineering, Shanghai Jiao Tong University, Shanghai, China

[2] Department of Cardiothoracic Surgery, Affiliated East Hospital of Xiamen University, Fuzhou, China

[3] Robarts Research Institute, Western University, London, Canada

due to their large diameter in relation to that of the bronchi [1]. Magnetic tracking (MT)-enabled navigation can be a useful adjunct to computed tomography (CT)-guided bronchoscopy biopsy of lung tumors [2]. With the overlap between the CT scan anatomy and the magnetic field, the positions of magnetic sensors embedded in the probe can be recorded in real time. The American College of Chest Physicians (ACCP) has recommended (electro)magnetic navigation bronchoscopy for patients who have a peripheral lung nodule [3].

Percutaneous biopsy is recognized as the standard of care for lung biopsy, where the pleura is punctured to reach the target tissue. This approach, however, relies heavily on the experience of the operator. Percutaneous biopsy also requires CT images to identify features such as blood vessel, to establish guidance plan. Technology such as ultrasound-guided or CT-guided approaches has been applied to assist percutaneous biopsy. Ultrasound-guided biopsy does not require the use of radiation, is readily available and is real time, but due to its application to the lung is limited unless the lung is collapsed. Therefore, CT-guided transthoracic approaches have been widely used to guide peripheral biopsy and thermal ablation of lung tumors [4]. However, CT-guided biopsy requires a series of CT scans to ensure that the probe properly approaches the target region, which introduces excessive radiation exposure for patient. Most research in this area has focused on automating the procedure [5,6]. Another limitation is that the patient is asked to suspend breathing during the biopsy process [7]. The biopsy system proposed in [8] can be applied to a patient respiration pattern by acquire several CT images acquired at different breathing phases, from which a relationship between breathing phase and skin surface motion can be determined. In addition, this approach also causes extra patient radiation exposure.

The methods that compensate for respiratory motion in precision radiotherapy can be existed in two categories: direct and indirect compensation. For the direct methods, X-ray imaging technology is applied to locate the target tumor. The patient must endure extra radiation dose during tumor tracking to obtain accurate results [9]. Indirect methods employ statistical analysis of the markers' position or tidal volume to determine the relationship between tumor motion and the external surrogate indicators of respiration. Yan et al. [10] placed external markers on patient's chest wall and developed a linear regression model to build the relevant relationship between tumor motion and external marker position. Low et al. [11] developed a mathematical model of motion to present the correlation between target motion and tidal volume for every volunteer and achieved an average error of $0.75 \pm 0.25$ mm. However, 15 CT scans were required in every experiment, resulting in a radiation dose level that is excessive for biopsy procedures. The simulation result of indirect compensation is not promised because the phase difference between internal tumor and external displacement of the chest and abdomen detected from body surface is not guaranteed to be equal during whole respiration [12].

Most of these navigation technologies of precision biopsy and radiotherapy are based on 3D CT reconstruction, just as percutaneous biopsy requires reconstructing CT images to mark the target and design puncture route. However, respiratory motion introduces uncertainties in the location, size and location of the tumor [13]. Furthermore, lung motion is complex and patient-specific. To resolve this problem, a number of studies have employed four-dimensional 4DCT [14–16]. With deformable image registration (DIR), 4DCT provides the possibility of depicting the change of target tumor position and shape at different respiratory phases, with various motion estimation methods having been proposed [15,16]. These techniques can be divided into geometric, image-based or biomechanical-based methods. For geometric approaches, feature landmarks are defined by surfaces, curves, lines and points in each image. Then computing a deformation vector field using such as minimize the difference between landmarks, to achieve a deformation vector field. For intensity-based methods, the deformation field is generated by minimizing or maximizing the correlation metrics in voxel- or patch-wise intensity patterns of images. Ehrhardt et al. [17] estimated the optical flow between the images at neighboring temporal patterns and generated a velocity field for different respiratory cycle based on a nonlinear registration. However, because 4DCT is a discontinuous imaging method, difficulties arise when attempting to accurately describe whole lung motion and its inevitable risks to both patient and technician due to the excessive radiation for the dynamic CT sequence acquisition. Additional comparison and evaluation of different registration approaches can be found in [18] and [19], and most of these methods achieve satisfactory results. However, neither geometric nor intensity-based methods take biological and physical characteristics into account [20].

On the other hand, biomechanically based methods aim to build a respiration motion model with those characteristics to simulate the deformation of lung tissue during breathing at different phases. Almost all biomechanically based methods are based on finite element methods (FEMs) that a require boundary conditions, accurate patient-specific organ meshes and patient-specific biological parameters, such as Young's modulus and Poisson's ratio, to track a target region. As distinct from intensity-based methods, FEM approaches rely on an energy function that can represent lung motion more realistically, instead of a similarity metric. For instance, Sundaram and Gee [21] entreated the FEM as a classic elastic matching technique to perform non-rigid registration, while another strategy is a force-driven approach. For instance, Fuerst et al. [22] described lung deformation driven by pre-defined surrounding thoracic negative forces. Due to the difficulties encountered to accurately describe biological properties, both of these approaches assume that the lung tissue is homogeneous.

In reality, most human organs are heterogeneous and subject-specific. Werner et al. [23] analyzed the relationship between lung motion and various elasticity parameters assigned to the lung tissue, revealing that the difference in assigned elasticity has little influence on the displacement field. On the other hand, Al-Mayah et al. [24] focused on the influence of the coefficient of friction and Poisson's ratio on respiration simulation that the error decreases with the increasing Poisson's ratio. As a result, the heterogeneity of the lung directly affects the accuracy of lung motion estimation, but it is impossible to achieve the particular biological properties of every individual patient in clinic. In order to present these properties, Li et al. [25] introduced a patient-specific and position-specific lung motion based on FEM, and correct the FEM mesh's elasticity distribution by invoking the quasi-Newton method. Using this approach, the inhomogeneous material property distribution will be achieved automatically. However, the FEM simulation is time consuming, even with GPU acceleration, taking around 500 s [25], which does not satisfy the requirements of clinical CT-guided biopsy.

In this paper, we focus on biomechanical-based lung dynamic motion modeling methods applied to CT-guided percutaneous biopsy. Our goal is to build a patient-specific biomechanical model that is suited to clinical biopsy. Therefore, we propose a patient-specific biomechanical model to describe lung respiratory motion based on the boundary element method (BEM). The boundary condition of BEM is achieved by a nonparametric discrete registration with convex optimization [26]. To achieve the goal of real-time simulation, we apply pre-computation to restore the coefficient in a matrix before surgery, which we believe to be the first BEM lung motion model for real-time clinical application. Since BEM models can only represent the motion of lung's surface during respiration, we also present a tetrahedron-based interpolation method to predict the respiratory motion of the internal lung tissue.

## Methods

### Method overview

A flow diagram of our BEM lung model scheme is shown in Fig. 1, which includes four main steps: (1) segmentation and reconstruction, (2) boundary condition acquisition, (3) BEM computation and parameter iteration and (4) tetrahedron-based interpolation. Our model comprises the surface of the lung and the vessel tree. Specially, the landmark points on the vascular tree are determined by experts. The lung surface motion computed by registration are used as the boundary conditions. Finally, a BEM motion model which can estimate both surface motion and internal motion is presented based on the tetrahedron-based interpolation method and the pre-compute algorithm.

### Segmentation and reconstruction

To begin, we enhance the edges of the ROI in CT using an intensity gradient detection algorithm, and then, a conventional 3D region growing method is used to extract the ROI. The extraneous tissue, such as ribs and the heart, is removed during this process, and the ROI is converted into a binary image. The gaps produced by vessels and bronchi are filled by dilating them with a 4–10-mm-diameter spherical structuring element (SE) [27]. Finally, these binary images and the original patient CTs are combined to generate new images that include biological information about the lung. The lung surface mesh model is reconstructed from the binary image by the conventional fast matching method. The vessel representation only needs to retain the branch points within the vessel tree. We using MIMICS (Version 10.01) to segment vessel tree by setting a global threshold vary from [418 1902]. For different data sets, this value need a slight adjustment based on histogram analysis.

### Boundary condition acquisition

Any position on the lung surface model will shift during the respiratory cycle. However, this motion is limited by biological forces such as surface or internal tension. In this subsection, we determine the restriction condition of lung surface motion via the multiresolution registration framework [26]. This surface motion of the lung is used as the boundary of our BEM model. To simplify the registration process, the registration computation is only restricted in the lung region (ROI). The motion of the lung surface, calculated from the displacement field of voxels, is employed as the boundary condition.

Let image pairs $I_{\mathrm{EI}}(x)$ and $I_{\mathrm{EE}}(\mathrm{x})$ be the EI image and EE image, respectively. The goal of this registration is to find the deformation vector $d$ for each voxel $x_i$ to minimize the cost function $F(d)$ formulated by patch-based similarity metrics [28].

$$F(d) = \sum_{x_i \in \Omega} \left[ I_{EI}(x_i) - I_{EE}(x_i + d) \right]^2 + \alpha \left| \nabla d \right|^2, \qquad (1)$$

where $\Omega$ represents an image patch for similarity term. Here $|\nabla d|$ is the gradient of the displacement vector. $\alpha$ is coefficient controlling the weights of the intensity term and the diffusive regularization term, and is implicitly defined in the Gaussian kernel. The search space of deformations is based on three resolution levels and the global deformation field

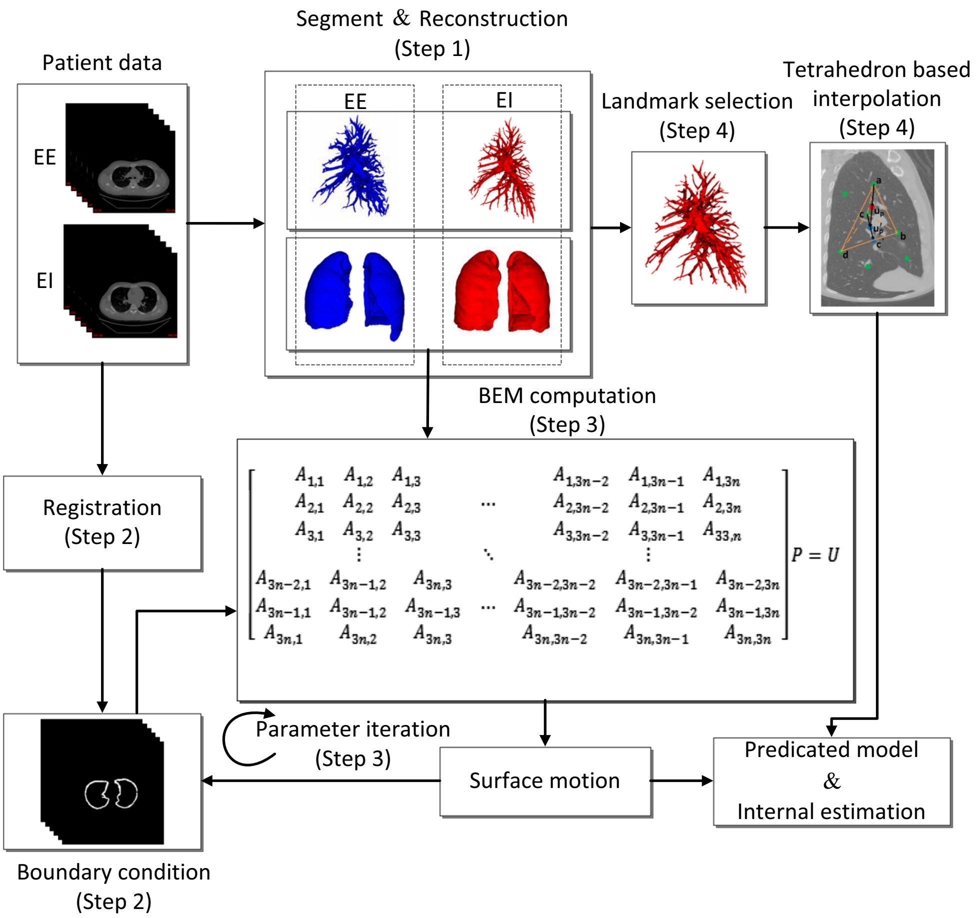

**Fig. 1** Framework of the BEM lung motion estimation

is smoothed through Gaussian convolution with the kernel in the first two resolution levels in order to improve the robustness of the registration procedure. Therefore, the final deformation field follows Eq. 1 without the regularization term and Gaussian smoothness, which is different from the registration method described in [26].

### The BEM respiratory motion surface model and parameter iteration

In this section, the patient-specific lung deformation estimation is an elasticity distribution problem. We aim to find the Young's modulus E and the coefficient of Poisson's ration to best marching the boundary condition from the registration. Here, we assume a uniform negative pressure is exerted on the lung surface and the interaction between the lung and other organs is ignored.

Elasticity theory demands six fundamental equations and boundary conditions, as shown in following equations,

$$\sigma_{ij,j} + f_i = 0 \tag{2}$$

$$\varepsilon_{ij} = \frac{1}{2}\left(u_{i,j} + u_{j,i}\right) \tag{3}$$

$$\varepsilon_{ij} = \frac{1+\nu}{E}\sigma_{ij} - \frac{\nu}{E}\sigma_{kk}\sigma_{ij} \tag{4}$$

$$\sigma_{ij} = 2G\varepsilon_{ij} + \lambda\varepsilon_{kk}\sigma_{ij} \tag{5}$$

$$p_i = \sigma_{ij}n_j = \bar{p}_i \tag{6}$$

$$u_i = \bar{u_i}, \tag{7}$$

where $\varepsilon_{ij}$ is the strain tensor, $\sigma_{ij}$ the stress tensor, $E$ is Young's modulus, $\upsilon$ the Poisson's ratio, $G$ is the shearing modulus of elasticity, $\lambda$ is the Lamé ratio, $f$ the volume force, while $u_i$ and $p_i$ are the unknown displacement and surface forces. $\bar{u_i}$ and $\bar{p}_i$ are the known displacement and surface forces.

We define the Kelvin fundamental solution of $u_i$ as $u^*(P, Q)$ and the Kelvin fundamental solution of $p_i$ as $p^*(P, Q)$. As for point $P$ and $Q$ on the lung surface, the Kelvin fundamental solution has the form as described in [29]:

$$u^*_{lk}(P, Q) = \frac{1}{16\pi\,(1-\upsilon)\,Gr}\left[(3-4\upsilon)\,\delta_{ij} + r_{,l}r_{,k}\right] \tag{8}$$

$$p^*_{lk}(P, Q) = -\frac{1}{8\pi\,(1-\upsilon)\,r^2}\left\{\frac{\partial r}{\partial n}\left[(1-2\upsilon)\,\delta_{lk} + 3r_{,l}r_{,k}\right] - (1-2\upsilon)\left(r_{,l}r_{,k} - r_{,k}r_{,l}\right)\right\} \tag{9}$$

In the above equations, $i, j, k = 1, 2, 3$ which denote the three direction in the coordinate systems. r represents the distance between $P$ and $Q$, $n$ is the normal of surface and $\delta$ is the Dirac delta function.

Based on Green's formulation, the discrete description of boundary integral equation at node $p_{\mathrm{i}}$ is represented by Eq. (10)

$$Cu_i + \sum_{j=1}^{N} \int_{\Gamma_j} p^* \, \mathrm{d}\Gamma \, u_j = \sum_{j=1}^{N} \int_{\Gamma_j} u^* \, \mathrm{d}\Gamma \, p_j \;\; (i = 1, 2, \ldots N), \tag{10}$$

where $C, p^*, u^*$ are $3 \times 3$ matrices. $u_i, u_j, p_j$ are $3 \times 1$ vectors. $\Gamma$ is the surface boundary and is divided into $N$ sub-elements $\Gamma_j$, and C represents the smoothness at $P_j$ is defined as: [30]

$$C = \begin{pmatrix} \frac{1}{2} & 0 & 0 \\ 0 & \frac{1}{2} & 0 \\ 0 & 0 & \frac{1}{2} \end{pmatrix} \tag{11}$$

Let $H_{ij} = C\delta_{ij} + \int_{\Gamma_j} p^* \mathrm{d}\Gamma$, $K_{ij} = \int_{\Gamma_j} u^* \mathrm{d}\Gamma$. Equation (10) is rearranged as:

$$\sum_{j=1}^{n} H_{ij} u_j = \sum_{j=1}^{n} K_{ij} p_{ij}, \tag{12}$$

More intuitively, Eq. (12) is rewritten as:

$$HU = KP \tag{13}$$

For $n$ nodes, the $H$ and $K$ is a $3n \times 3n$ matrix, with $U$ and $P$ representing the displacement and external force. After rearrangement, we obtain:

$$HU = KP \Rightarrow U = H^{-1}KP = AP \Rightarrow P = A^{-1}U \tag{14}$$

The displacement of each node is computed using Eq. (14), where the matrix A is pre-computed.

The strategy to find patient-specific and position-specific matrix $\widehat{A_n}$ to match boundary condition is an optimization process and can be obtained using Eq. (15).

$$\widehat{A_n} = \arg\min_{A \in \Re} \left\{ \Phi(A) = \frac{1}{2} U_{\mathrm{B}}(A) - U_R^2 \right\} \tag{15}$$

Here $U_{\mathrm{B}}$ represents the displacements generated by the BEM and $U_{\mathrm{R}}$ represents the boundary condition which is interpolated by the displacement of lung surface points.

Firstly, we update Young's modulus $E$ with the coefficient of Poisson's ratio remaining unchanged. We take a Taylor series of the differential of the function (15) at $E_k$ and obtain a new equation:

$$[U_{\mathrm{B}},]^T (U_{\mathrm{B}} - U_{\mathrm{R}}) + [U_{\mathrm{B}},]^T \left[U'_{\mathrm{B}}\right] \Delta E_k = 0 \tag{16}$$

Since the external force $P$ is independent of Young's modulus $E$, we take the partial derivative to Eq. (14),

$$\frac{\partial P}{\partial E} = \frac{\partial A^{-1}}{\partial E} U + A^{-1} \frac{\partial U}{\partial E} \Rightarrow \frac{\partial A^{-1}}{\partial E} U_{\mathrm{B}} + A^{-1} \frac{\partial U_{\mathrm{B}}}{\partial E} = 0 \tag{17}$$

Therefore, the corresponding $E$ can be updated iteratively by Eqs. (16) and (17).

Similarly, we update the coefficient of Poisson's ratio while keeping Young's modulus $E$ unchanged. Each optimal solution is iteratively computed until it approaches an ideal value of $\Delta U_{\mathrm{B}} < 0.4\,\mathrm{mm}$, for each surface point of the BEM model.

## Tetrahedron-based interpolation method

Even though the BEM model can efficiently simulate the surface motion, tumors are not always located on the lung surface. In this section, tetrahedron-based interpolation method is employed to predict the internal tissue's motion during entire breathing cycle.

Expert-determined landmark points (Fig. 2) and all vertexes of the lung surface model are used to generate a volumetric model with tetrahedron elements by TetGen [31]. The position of the unknown point ($u_p$) and the tetrahedron that contained $u_p$ are shown in Fig. 3. The deformation information of $u_p$ is generated based on the geometrical relationship between locations of four vertexes $(a, b, c, d)$ and $u_p$.

$$\begin{aligned} \overrightarrow{au_p} &= m\overrightarrow{au'_p} = m\left(\overrightarrow{ac} + \overrightarrow{ncc'}\right) = m\left(\overrightarrow{ac} + n\left(\overrightarrow{cb} + k\overrightarrow{bd}\right)\right) \\ &= m\overrightarrow{ac} + mn\overrightarrow{cb} + mnk\overrightarrow{bd}, \end{aligned} \tag{18}$$

where $m = \frac{D(a,u_p)}{D\left(a,u'_p\right)}$, $n = \frac{D\left(c,u'_p\right)}{D(c,c'))}$ and $k = \frac{D(b,c'))}{D(b,d)}$ are scale factors determined by the Euclidean distance $D$ between two points. $u'_p$ is the projection position of $u_p$ on the boundary face $S_{\Delta bcd}$. We represent the vector by the individual position $x = [x_1, x_2, x_3]^T$ of each vertex, and Eq. 18 is rewritten as:

$$x_{u_p} - x_a = m(x_c - x_a) + mn(x_b - x_c) + mnk(x_d - x_b), \tag{19}$$

$$x_{u_p} = (1-m)\,x_a + mn(1-k)\,x_b + m(1-n)\,x_c + mnkx_d, \tag{20}$$

Therefore, the displacement $U_{u_p}$ of $u_p$ is generated by the tetrahedron-based interpolation as:

$$U_{u_p} = (1-m)\,U_a + mn(1-k)\,U_b + m(1-n)\,U_c + mnkU_d, \tag{21}$$

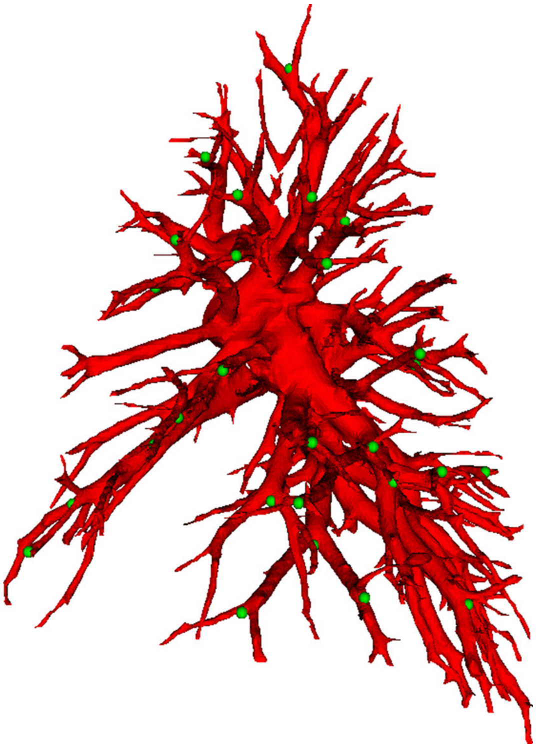

**Fig. 2** Vessel of EI phase and expert-determined landmark points (*green* spheres)

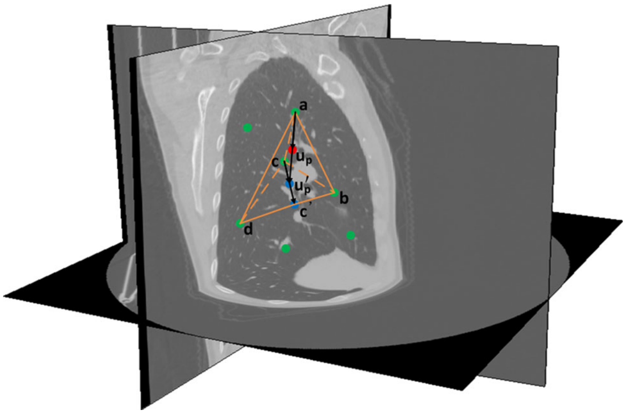

**Fig. 3** Location of an unknown point (*red disk*), expert-determined landmarks (*green disks*) and the tetrahedron element used to the tetrahedron-based interpolation

where $U_a$, $U_b$, $U_c$ and $U_d$ are spatial displacements of vertexes of the tetrahedron element, respectively. Notice that those spatial displacements can be provided by the BEM motion model and the motions of expert-determined landmarks due to all vertexes of tetrahedron elements in the volumetric model are constructed by expert-determined landmarks and the BEM lung surface vertexes.

## Experimental results

### Patient data preparation

In our framework, ten CT data sets were used to evaluate our BEM lung model. Cases 1 and 2 have a slice thickness of 1.25 mm, image dimension of $512 \times 512 \times 265$, while cases 3 and 4 have slice thicknesses of 5mm, resulting in a $512 \times 512 \times 67$ voxel matrix. All of these data sets were acquired from Fuzhou General Hospital and generated by a SIEMENS SOMATOM spirit dual-slice CT. The remaining data were acquired from the Léon Bérard Cancer Center & CREATIS laboratory [32], and possess the characteristic as detailed in Table 1. Cases 1–7 only recorded images in EE and EI phases and identified reference points in two breath phases. In the reference data, cases 8–10, 10 breath phases were acquired to evaluate the accuracy model of our model during breathing. Full details of the image data are shown in Table 1.

All the patients' lung surface models and vessel trees were segmented and constructed using the scheme we presented previously, and one of the ten lung surface models and its vessel tree are presented Fig. 4. In cases 1–4, landmarks are determined from the bifurcation points of vessels by the expert. In the remainder of the cases, the landmark points were identified using the software proposed by Murphy et al. [33].

The BEM models were computed in C++ on a desktop PC with a quad-core 2.0 GHz processor and 10GB RAM. Table 2 illustrates the number of landmark points that were used for the tetrahedron-based interpolation, characteristics of BEM and computation time for left lung (LL) and right lung (RL) of each case, where the case meshed with a fewer nodes and triangles maintains a fast computation and a higher update rate. The parameters of the registration for all cases and the clinical experiment are: the standard deviation of Gaussian kernel $\sigma = 0.6$ and the radius of patch-based similarity metrics $r = 2$.

### Prediction of surface and internal motion based on landmarks for each case

In this section, the prediction error between the BEM mesh model and the segmented model from data sets acquired in the end inspiration state is investigated as shown in Fig. 5.

We employ the mean error and the standard deviation of the TRE and the ASSD [34] to assess the result of BEM estimation with the tetrahedron-based interpolation as shown in Table 3. The TRE is computed from the Euclidean distances between the landmark's estimated position and its

**Table 1** Characteristics of data sets for each case

| Case | Number of breath phases | Tidal volume (ml) | Image dimensions | image resolution (mm) |
|---|---|---|---|---|
| 1 | 2 | 655.5 | 512 × 512 × 265 | 0.912 × 0.912 × 1.25 |
| 2 | 2 | 589.4 | 512 × 512 × 265 | 0.936 × 0.936 × 1.25 |
| 3 | 2 | 586.9 | 512 × 512 × 67 | 0.912 × 0.912 × 5 |
| 4 | 2 | 558.2 | 512 × 512 × 67 | 0.912 × 0.912 × 5 |
| 5 | 2 | 392.9 | 512 × 512 × 140 | 1.1719 × 1.1719 × 2 |
| 6 | 2 | 444.3 | 512 × 512 × 187 | 0.7813 × 0.7813 × 2 |
| 7 | 2 | 182.2 | 512 × 512 × 161 | 1.1719 × 1.1719 × 2 |
| 8 | 10 | 644.2 | 512 × 512 × 169 | 0.9766 × 0.9766 × 2 |
| 9 | 10 | 217.0 | 512 × 512 × 141 | 0.9766 × 0.9766 × 2 |
| 10 | 10 | 396.9 | 512 × 512 × 170 | 0.8789 × 0.8789 × 2 |

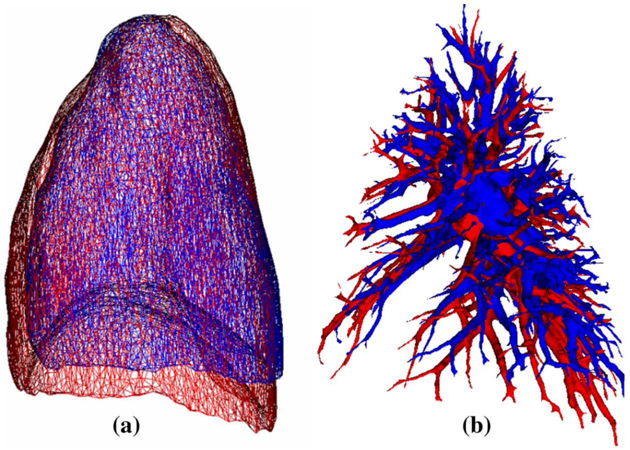

**Fig. 4** Lung model and vessel tree of case 1 between EE phase (*blue*) and EI phase (*red*). **a** Overlay of lung surface model, **b** vessel tree

position at the target phase. Note that the target phase in Table 3 is the maximal inhalation while in Fig. 6 the target phase is determined by the tidal volume. The TRE of the results using 10 landmarks to construct the volumetric model, the minimum Jacobian value (($J_{\min}$) and the maximum Jacobian value (($J_{\max}$) for the vector-valued transformation $h(x) = [h_1(x), h_2(x), h_3(x)]^T$ of a location $x = (x_1, x_2, x_3)^T$ are listed in Table 4. The determinant of the Jacobians of the deformation field is defined as:

$$J(h(x)) = \begin{vmatrix} \frac{\partial h_1(x)}{\partial x_1} & \frac{\partial h_2(x)}{\partial x_1} & \frac{\partial h_3(x)}{\partial x_1} \\ \frac{\partial h_1(x)}{\partial x_2} & \frac{\partial h_2(x)}{\partial x_2} & \frac{\partial h_3(x)}{\partial x_2} \\ \frac{\partial h_1(x)}{\partial x_3} & \frac{\partial h_2(x)}{\partial x_3} & \frac{\partial h_3(x)}{\partial x_3} \end{vmatrix} = \begin{vmatrix} 1 + \frac{\partial u_1(X)}{\partial X_1} & \frac{\partial u_2(X)}{\partial X_1} & \frac{\partial u_3(X)}{\partial X_1} \\ \frac{\partial u_1(X)}{\partial X_2} & 1 + \frac{\partial u_2(X)}{\partial X_2} & \frac{\partial u_3(X)}{\partial X_2} \\ \frac{\partial u_1(X)}{\partial X_3} & \frac{\partial u_2(X)}{\partial X_3} & 1 + \frac{\partial u_3(X)}{\partial X_3} \end{vmatrix}, \quad (22)$$

**Table 2** Details of the BEM model for each case

| Case | | Number of landmarks | | Node (triangles) | Computation time | | | Update rate (fps) |
|---|---|---|---|---|---|---|---|---|
| | | Total | Tetrahedron-based interpolation | | Lung segmentation | Registration | Pre-computed BEM model | |
| 1 | RL | 45 | 5/10 | 5423 (10842) | 167 s | 30 min | 301 s | 21 |
| 2 | RL | 47 | 5/10 | 4467 (8930) | 159 s | 28 min | 212 s | 33 |
| 3 | RL | 45 | 5/10 | 4588 (9172) | 40 s | 13 min | 248 s | 31 |
| 4 | RL | 40 | 5/10 | 4632 (9260) | 42 s | 12 min | 274 s | 30 |
| 5 | RL | 51 | 5/10 | 4443 (8882) | 85 s | 15 min | 232 s | 34 |
| 6 | RL | 65 | 5/10 | 4888 (9810) | 98 s | 20 min | 289 s | 28 |
| 7 | RL | 65 | 5/10 | 5056 (10118) | 91 s | 15 min | 357 s | 25 |
| 8 | RL | 56 | 5/10 | 4621 (9251) | 92 s | 20 min | 300 s | 30 |
| | LL | 44 | 5/10 | 4267 (8836) | | | 279 s | 33 |
| 9 | RL | 40 | 5/10 | 4547 (9195) | 84 s | 13 min | 287 s | 32 |
| | LL | 60 | 5/10 | 4196 (8590) | | | 273 s | 34 |
| 10 | RL | 62 | 5/10 | 48,127 (95,121) | 95 s | 18 min | 2604 s | 13 |
| | LL | 38 | 5/10 | 45,601 (92,158) | | | 2511 s | 13 |

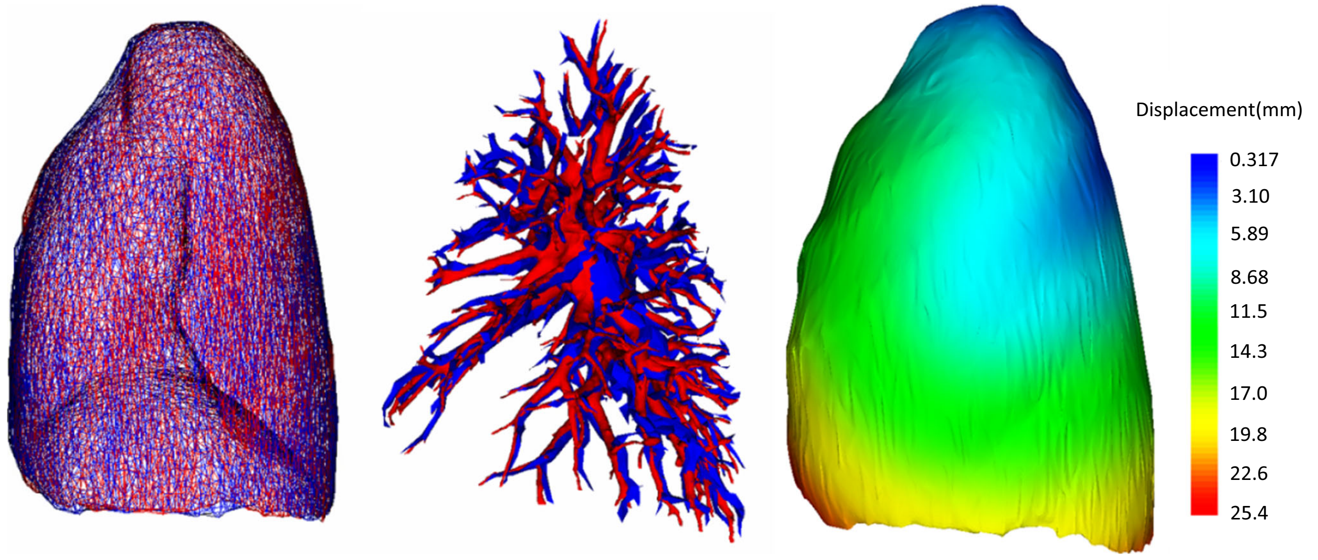

(a) (b) (c)

**Fig. 5** Estimation result of the BEM and interpolation. **a** Lung surface model result, **b** vessel tree result, **c** visualization of displacement (mm)

**Table 3** Mean error (standard deviation) of surface and landmark points (mm)

| Case | | Mean displacement | ASSD of the registration | ASSD of the BEM | TRE (Num:10) | TRE (Num:5) |
|---|---|---|---|---|---|---|
| 1 | RL | 14.6 | 1.9 (1.8) | 1.8 (1.7) | 2.1 (1.9) | 2.5 (3.0) |
| 2 | RL | 13.1 | 1.7 (1.9) | 1.6 (1.8) | 2.0 (1.8) | 2.3 (2.4) |
| 3 | RL | 13.1 | 1.9 (1.8) | 1.8 (2.0) | 2.5 (2.1) | 3.2 (3.1) |
| 4 | RL | 12.5 | 1.8 (2.0) | 1.7 (1.9) | 2.1 (1.9) | 2.8 (2.7) |
| 5 | RL | 10.9 | 1.6 (1.1) | 1.5 (1.0) | 1.8 (1.4) | 2.2 (2.2) |
| 6 | RL | 9.4 | 1.5 (1.5) | 1.4 (1.3) | 1.6 (1.4) | 1.8 (2.1) |
| 7 | RL | 4.1 | 1.2 (1.1) | 1.0 (0.9) | 1.2 (1.3) | 1.3 (1.6) |
| 8 | RL | 14.9 | 1.7 (1.0) | 1.8 (1.0) | 2.2 (1.7) | 2.7 (1.9) |
| | LL | 15.7 | 1.9 (1.0) | 1.9 (0.8) | 2.5 (1.8) | 3.1 (2.4) |
| 9 | RL | 6.5 | 1.3 (0.8) | 1.2 (0.8) | 1.1 (0.9) | 1.6 (1.4) |
| | LL | 6.9 | 1.6 (1.4) | 1.3 (1.2) | 1.3 (1.2) | 1.7 (1.6) |
| 10 | RL | 9.1 | 1.6 (1.1) | 1.3 (1.0) | 1.6 (1.4) | 2.0 (1.7) |
| | LL | 9.9 | 1.7 (1.2) | 1.4 (1.1) | 1.8 (1.6) | 2.6 (2.0) |

where $h_1(x)$ is the x component of $h(x)$ in left–right direction, $h_2(x)$ is the y component of $h(x)$ in anterior–posterior direction and $h_3(x)$ is the z component of $h(x)$ in superior–inferior direction. $x_1, x_2$ and $x_3$ are the three components of a location x, respectively. $u(x) = [u_1(x), u_2(x), u_3(x)]^T$ is the corresponding displacement performs the foliation image to the target image.

As our motion model is reconstructed from two breath phases, we used the data sets of CREATIS to validate the performance of our model during the respiratory process and the TRE of the analysis of the nine respiratory phrases of cases 8–10 is summarized in Fig. 6.

## Biopsy clinical experiment

Two clinical biopsy experiments were performed to further validate our method in a CT-/MT-guided biopsy application. The clinical biopsy environment includes: a CT scanner, a magnetic tracking system, navigation software and probe with sensor as shown in Fig. 7. An Aurora magnetic tracking (Northern Digital Inc.) device, employing a flat tabletop magnetic field generator, and with the accuracy of 0.48 mm RMS, was used to track the position of the puncture needle. The lung CT data sets at two phases were generated by a SIEMENS SOMATOM Spirit dual-slice CT with a slice

**Fig. 6** TRE of each tidal volume of case 8–10. **a** TRE of case 8, **b** TRE of case9 and **c** TRE of case10

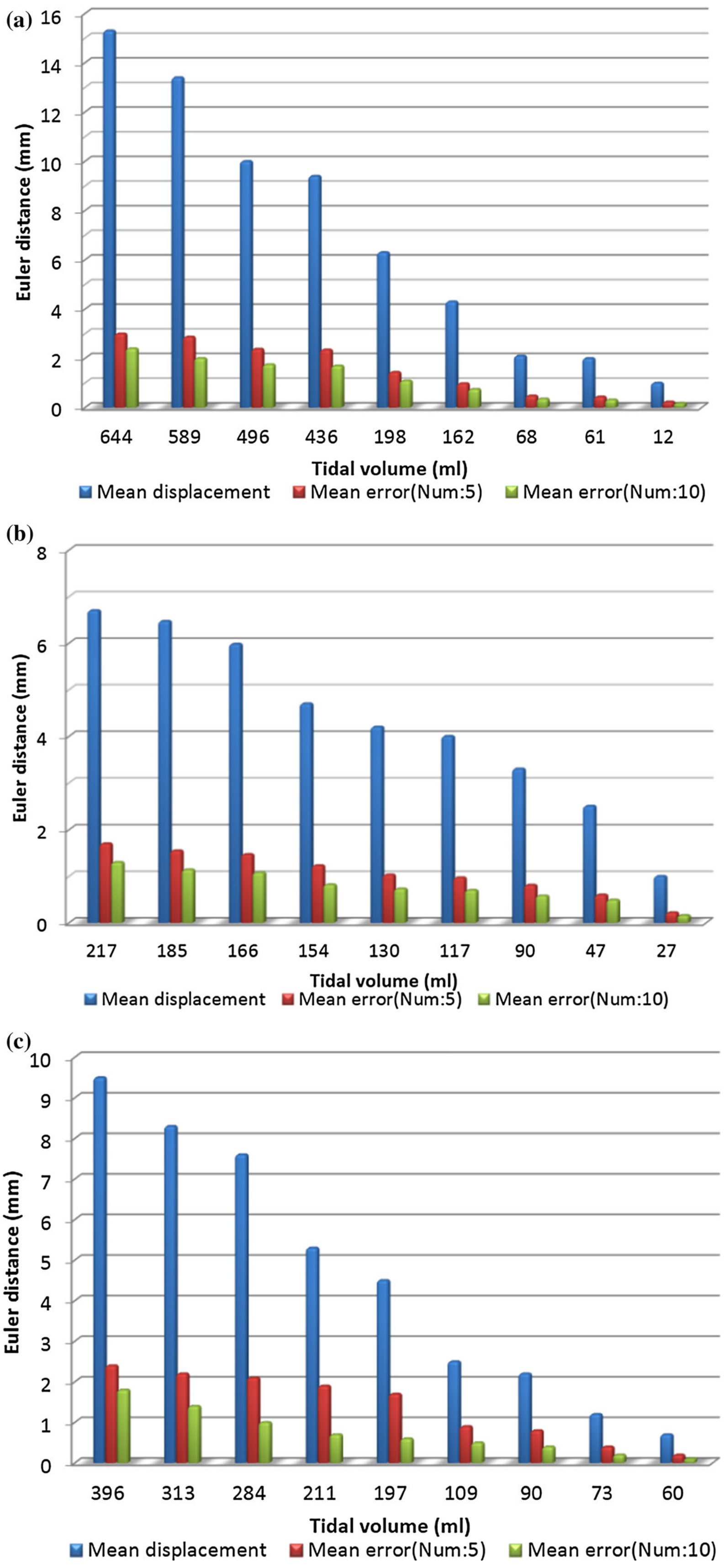

**Table 4** Mean TRE (standard deviation) of the result using 10 landmark points to construct the volumetric model. The minimum Jacobian value ($J_{\min}$) and the maximum Jacobian value ($J_{\max}$) for each deformation field are also listed

| Case | | The mean TRE (standard deviation) (mm) | | | | The Jacobian value | |
|---|---|---|---|---|---|---|---|
| | | 3D-Euclidean | Craniocaudal | Anteroposterior | Left–right | $J_{\min}$ | $J_{\max}$ |
| 1 | RL | 2.1 (1.9) | 1.4 (1.4) | 0.6 (0.5) | 1.1 (1.1) | 0.79 | 2.47 |
| 2 | RL | 2.0 (1.8) | 1.4 (1.3) | 0.5 (0.5) | 1.0 (1.2) | 0.78 | 2.24 |
| 3 | RL | 2.5 (2.1) | 1.7 (1.5) | 1.3 (1.1) | 0.9 (0.8) | 0.83 | 2.16 |
| 4 | RL | 2.1 (1.9) | 1.4 (1.2) | 0.7 (0.6) | 1.1 (1.0) | 0.81 | 2.12 |
| 5 | RL | 1.8 (1.4) | 1.0 (1.4) | 0.7 (0.9) | 0.9 (1.3) | 0.85 | 2.02 |
| 6 | RL | 1.6 (1.4) | 1.0 (1.0) | 0.6 (0.4) | 0.7 (1.2) | 0.87 | 1.99 |
| 7 | RL | 1.2 (1.3) | 1.0 (1.2) | 0.4 (0.7) | 0.3 (0.5) | 0.93 | 1.67 |
| 8 | RL | 2.2 (1.7) | 1.5 (1.6) | 0.6 (0.5) | 1.1 (1.0) | 0.85 | 2.08 |
| | LL | 2.5 (1.8) | 1.6 (1.6) | 1.3 (1.1) | 0.9 (0.7) | 0.87 | 2.23 |
| 9 | RL | 1.1 (0.9) | 0.8 (0.9) | 0.5 (0.5) | 0.6 (0.7) | 0.74 | 1.76 |
| | LL | 1.3 (1.2) | 0.8 (1.0) | 0.6 (0.4) | 0.7 (0.9) | 0.82 | 1.63 |
| 10 | RL | 1.6 (1.4) | 1.0 (1.1) | 0.7 (0.4) | 0.6 (1.1) | 0.85 | 1.87 |
| | LL | 1.8 (1.6) | 1.2 (1.3) | 0.5 (0.4) | 0.5 (0.8) | 0.86 | 1.83 |

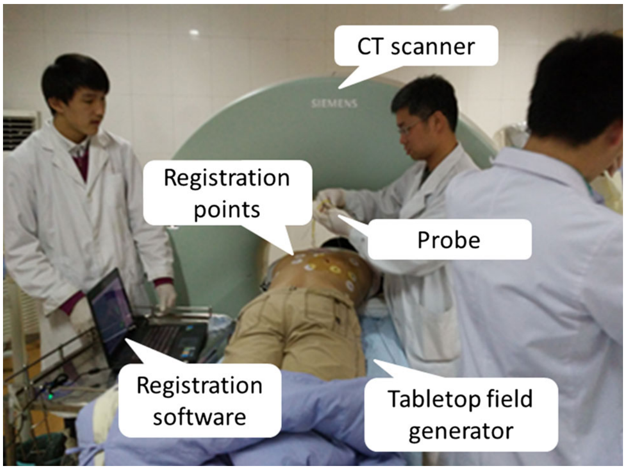

**Fig. 7** Biopsy environment

thickness of 3.0 mm and image dimension of 512 × 512 × 48. The clinical experiment has the approval of the institutional ethics committee (certificate number FZY20160605N016).

The lung motion model was generated based on Step (1)–(4) as shown in Fig. 1. During the biopsy procedure, those patient-specific biological parameters are directly loaded from memory during the respiration simulation. Since the motion of the lung surface can be simulated without recomputation, we only need to calculate the tetrahedron-based interpolation method with preoperative selection of vessel bifurcations to correct the motion of blood vessels and suspicious lung tissue regions.

Eight fiducial markers fixed to the patient's skin are detected by the operator and used for surface registration. The first CT scan was taken after a reference needle has pierced the lung, based on preoperative CT images and the experience of a thoracic surgeon. Since we have simulated the breathing motion of the lung surface in whole breathing cycle before the operation, the respiratory phase at the time of the first CT scan can be determined based on the lung surface profile in the first CT scan. Then the position of the reference needle in our BEM model can be computed at the corresponding phase, and this position will be modified based on the actual position of the reference needle in CT images. Therefore, the precision of motion detection near the reference needle will be improved. The movement of the reference needle during the biopsy is achieved by the magnetic tracker and is employed to synchronize our BEM model with the actual patient breathing cycle. Since the reference needle has been pierced close to the target region, we assume that the hysteresis of the target region can be presented by the reference needle. In addition, the variations of the breathing amplitude and breathing rate are also presented by the motion of reference needle. Theoretically, the closer the reference needle is to the target position, greater the precision of the navigation system. With the assistance of the magnetic tracker and the prediction of the lung motion model, the probe may be accurately guided to the target. The target position of biopsy is determined by the thoracic surgeon as shown in Fig. 8. A second CT is acquired to validate the final puncture result. The model-based prediction error (TRE) for the respiratory motion in two clinical experiments are 3.1 mm (tumor volume: 12.62 cm$^3$, tumor motion: 15.3 mm) as shown in Fig. 8 and 2.0 mm (tumor volume: 8.76 cm$^3$, tumor motion: 11.4 mm), respectively. These results demonstrate that the described framework is appropriate to fulfill the requirements of real-time image-guided biopsy.

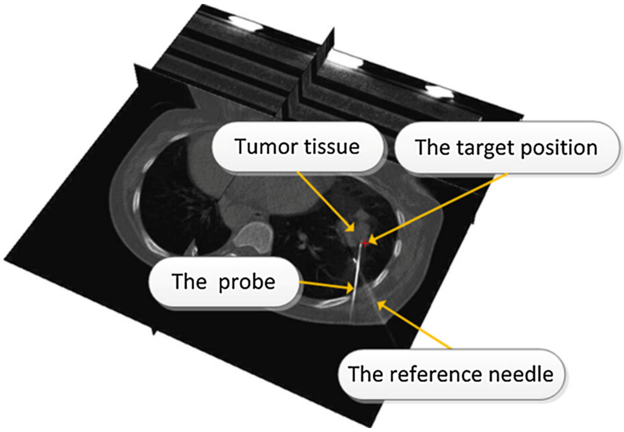

**Fig. 8** Result of the biopsy clinical experiment

## Discussion

In order to realize a real-time lung motion simulation for clinical lung needle biopsy, we presented a BEM model to simulate the motion of surface of the lung and employed the tetrahedron-based interpolation to estimate the motion of internal tissue. As shown in Table 3, the ASSD and the TRE ranged from 1.0 (0.9) to 1.9 (0.8) mm and 1.1 (0.9) mm to 2.5 (2.1) mm, respectively. For each case, the TRE using 10 landmarks to construct the volumetric model is 2.5 (2.1) mm at largest, while 3.2 (3.1) mm for 5 landmarks. The main parameters of the registration are: the standard deviation of Gaussian kernel $\sigma$ and the radius of patch-based similarity metrics $r$. Although the registration results are influenced by parameter variation in [26], the results of BEM simulation in this study are not sensitive to these parameters for three reasons. Firstly, the deformation of the lung surface can be easily achieved by registration because the lung region has been extracted before the registration process. Secondly, the smoothness parameter affects only on the first two registration levels and the final deformation field is generated by minimizing the dissimilarity between image pairs. Finally, the registration only provides the boundary condition for the BEM model. We have tuned the parameters of the registration to examine the influence of the parameters for each case. In case 1, the ASSD of the registration ranged from 1.9 (1.8) to 2.0 (1.9) mm and that produced by the BEM estimation method ranged from 1.8 (1.7) to 1.9 (1.8) mm for $0.3 \leq \sigma \leq 1.0$. The best and worst values of $r$ are 2 and 0, which results in 1.8 (1.7) and 1.8 (1.8) mm for the BEM simulation, respectively. In other cases, the best results are achieved when $\sigma \approx 0.6$ and $r = 2$. As shown in Table 3, the standard deviation of the ASSD of the presented BEM model is always smaller than that produced by the registration due to the motion constraint caused by the biomechanical model.

The tetrahedron-based interpolation is employed to predict the respiratory motion of the internal lung tissue. Suppose that there have two unknown points located on the different side of the boundary face of the tetrahedron element and they are closed to each other, we can derive that projection positions of these two unknown points on the boundary face are nearly overlap, further demonstrating that scale factors ($m$, $n$ and $k$) in Eq. 21 are approximately equal. Therefore, displacements of these two unknown points are both determined based on motions of three vertexes of the boundary face such that the tetrahedron-based interpolation method can ensure a continuous deformation magnitude distribution close to the boundary face of the tetrahedron element. Thus, a continuous lung surface and lung vessel model is generated as shown in Fig. 5. The clinical experimental results reveal that the BEM motion model adequately predicts the shift of the internal tissue.

In order to achieve the lung respiration simulation and predication of the target position in real time, patient-specific biological parameters are stored in a matrix in advance. The motion of the lung surface points is driven by the negative elastic force toward the target position. In each time step, the target positions are calculated from the pre-computed matrix. The coordinates of the EM tracker have been registered with the physical coordinate of fiducial markers attached on patient's skin. Therefore, the movement of the reference needle during the biopsy can be measured by the magnetic tracker, and this information can be employed to determine the respiratory phases in real time. This approach demonstrates that our BEM model can operate in real time to improve surgical outcome as well as to reduce patient radiation dose.

Fortmeier et al. [35] proposed an approach for real-time prediction of patient's individual respiratory motion based on 4D CT data, which is not applicable in our biopsy study. Restricted by the clinical availability, of CT, our method is only based on EE and EI phase CT data pairs, to reduce the patient radiation dose and cost. In addition, the breathing motion model in [35] was applied to a needle puncture training simulation framework, which ignores tissue motion hysteresis, and assume that breathing motion is a robust and fully reproducible. In contrast, in our method, the hysteresis near the target position and the breathing amplitude were reflected by the tracked motion of the reference needle. Comparing our results to a biophysical FEM approach for patient-specific modeling of breathing motion estimation [25], we note that the TRE of the BEM-based approach is comparable in internal tissue for similar tidal volumes, where the TRE is 2.1 (1.9) mm for the tidal volume is 655 ml when the average landmark displacement is 14.6 mm. The BEM model with the tetrahedron-based interpolation in this paper was presented with the aim of reducing the FEM simulation complexity for whole lung respiratory motion. Since BEM simulation only depends on the lung boundary, no computation resources are needed to update the whole volume. FEM simulation takes 10 h for a volumetric mesh with 108,387 nodes [25], while in contrast, the total time for our BEM simulation with 48,127 and 45,601 nodes is 1.4 h, as shown in Table 2. In addition, our approach performs in real time with the pre-computation strategy.

As distinct from the methods presented in [18,19], the goal of this study is to design an applicable, convenient and real-time method for routine clinical biopsy without requiring the patient to hold his breath. In order to improve the simulation efficiency, the respiratory motion modeling we present here places its focus on the lung surface, the position of the reference needle and the ROI (target suspicious tissue and blood vessels) rather than other normal tissue regions. Therefore, we only pre-compute the BEM of the lung surface and some of landmark points on blood vessels. To achieve the goal of reducing the preparation time, our nonparametric discrete registration incorporating a convex optimization approach achieved the best performance, with an approximate accuracy on the boundary, compared to 15 other state-of-the-art nonlinear registration methods [18]. This approach was employed to extract the lung surface motion, which is used as the boundary conditions of BEM model, achieving a competitive experimental result of TRE $\leq$ 2.5(2.1) mm as shown in Table 3, enabling a clinically acceptable update rate of 13 fps without GPU acceleration.

## Conclusions

In this study, a novel framework for patient-specific and position-specific respiratory motion simulation was proposed for image-guided lung biopsy, using a BEM model. Specifically, biomechanical parameters including Young's modulus and Poisson's ratio are incorporated within a pre-computed mixing coefficient. Due to the limitations of the BEM when applied to lung motion, we compensated the motion prediction with the tetrahedron-based interpolation method to predict the internal tissue vector field. By employing a pre-computed matrix of motion parameters, the BEM-based simulation model is able to run in real time allowing a target region (such as a tumor or pulmonary nodule) to be tracked during image-guided intervention. The result revealed that the errors of both surface and internal structures are clinically acceptable.

Our future study will address motion simulation of special cases such as lung atrophy and pneumothorax. Moreover, in order to reduce the radiation exposure to the patient using multiphase CT Scans, we will explore the use of a statistical model, building a database for the lung BEM models, where a single patient CT scan is employed to achieve a similar BEM model to simulate lung respiration deformation.

**Acknowledgements** This research is partially supported by the National Key research and development program (2016YFC0106200), 863 national research fund (2015AA043203), the Chinese NSFC research fund (61190120, 61190124 and 61271318) as well as Fujian Provincial Department of Science and Technology (2016Y0069). The authors thank the Léon Bérard Cancer Center & CREATIS laboratory for providing the 4DCT data.

### Compliance with ethical standards

**Conflict of interest** The authors declares that they have no conflict of interest.

**Ethical standard** All procedures performed in studies involving human participants were in accordance with the 8 ethical standards of the institutional and/or national research committee and with the 1964 Helsinki Declaration and its later amendments or comparable ethical standards.

**Informed consent** Informed consent was obtained from all individual participants included in the study.

## References

1. Kuntz A, Torres LG, Feins RH, Webster RJ, Alterovitz R (2015) Motion planning for a three-stage multilumen transoral lung access system. IEEE Int Conf Intell Robot Syst. doi:10.1109/IROS.2015.7353829
2. Arenberg D (2009) Electromagnetic navigation guided bronchoscopy. Cancer Imaging 9:89–95. doi:10.1102/1470-7330.2009.0016
3. Detterbeck FC, Lewis SZ, Diekemper R, Addrizzo-Harris D, Alberts WM (2013) Executive summary: diagnosis and management of lung cancer, 3rd ed: American College of chest physicians evidence-based clinical practice guidelines. Chest J 143:7S–37S. doi:10.1378/chest.12-2377
4. Eom J, Xu XG, De S, Shi C (2010) Predictive modeling of lung motion over the entire respiratory cycle using measured pressure-volume data, 4DCT images, and finite-element analysis. Med Phys 37:4389–4400. doi:10.1118/1.3455276
5. Fichtinger G, Deguet A, Masamune K, Balogh E, Fischer GS, Mathieu H, Taylor RH, Zinreich SJ, Fayad LM (2005) Image overlay guidance for needle insertion in CT scanner. IEEE Trans Biomed Eng 52:1415–1424. doi:10.1109/TBME.2005.851493
6. Hanumara NC, Walsh CJ, Slocum AH, Gupta R, Shepard JA (2007) Human factors design for intuitive operation of a low-cost, image-guided, tele-robotic biopsy assistant. In: Annual international conference of the IEEE engineering in medicine and biology proceedings, pp 1257–1260
7. Yang W, Sun W, Li Q, Yao Y, Lv T, Zeng J, Liang W, Zhou X, Song Y (2015) Diagnostic accuracy of CT-guided transthoracic needle biopsy for solitary pulmonary nodules. PLoS ONE 10:e0131373. doi:10.1371/journal.pone.0131373
8. Zhou Y, Thiruvalluvan K, Krzeminski L, Moore WH, Xu Z, Liang Z (2013) CT-guided robotic needle biopsy of lung nodules with respiratory motion—experimental system and preliminary test. Int J Med Robot Comput Assist Surg 9:317–330. doi:10.1002/rcs.1441
9. Keall PJ, Mageras GS, Balter JM, Emery RS, Forster KM, Jiang SB, Kapatoes JM, Low D a, Murphy MJ, Murray BR, Ramsey CR, Van Herk MB, Vedam SS, Wong JW, Yorke E (2006) The management of respiratory motion in radiation oncology report of AAPM Task Group 76. Med Phys 33:3874–3900. doi:10.1118/1.2349696

10. Yan H, Yin F-F, Zhu G-P, Ajlouni M, Kim JH (2006) The correlation evaluation of a tumor tracking system using multiple external markers. Med Phys 33:4073–4084. doi:10.1118/1.2358830
11. Low DA, Nystrom M, Kalinin E, Parikh P, Dempsey JF, Bradley JD, Mutic S, Wahab SH, Islam T, Christensen G, Politte DG, Whiting BR (2003) A method for the reconstruction of four-dimensional synchronized CT scans acquired during free breathing. Med Phys 30:1254–1263. doi:10.1118/1.1576230
12. Ozhasoglu C, Murphy MJ (2002) Issues in respiratory motion compensation during external-beam radiotherapy. Int J Radiat Oncol Biol Phys 52:1389–1399. doi:10.1016/S0360-3016(01)02789-4
13. Dawson LA, Jaffray DA (2007) Advances in image-guided radiation therapy. J Clin Oncol 25:938–946. doi:10.1200/JCO.2006.09.9515
14. Guerrero T, Sanders K, Castillo E, Zhang Y, Bidaut L, Pan T, Komaki R (2006) Dynamic ventilation imaging from four-dimensional computed tomography. Phys Med Biol 51:777–791. doi:10.1088/0031-9155/51/4/002
15. Vinogradskiy YY, Castillo R, Castillo E, Chandler A, Martel MK, Guerrero T (2012) Use of weekly 4DCT-based ventilation maps to quantify changes in lung function for patients undergoing radiation therapy. Med Phys 39:289–298. doi:10.1118/1.3668056
16. Ding K, Bayouth JE, Buatti JM, Christensen GE, Reinhardt JM (2010) 4DCT-based measurement of changes in pulmonary function following a course of radiation therapy. Med Phys 37:1261–1272. doi:10.1118/1.3312210
17. Ehrhardt J, Werner R, Säring D, Frenzel T, Lu W, Low D, Handels H (2007) An optical flow based method for improved reconstruction of 4D CT data sets acquired during free breathing. Med Phys 34:711–721. doi:10.1118/1.2431245
18. Werner R, Schmidt-Richberg A, Handels H, Ehrhardt J (2014) Estimation of lung motion fields in 4D CT data by variational non-linear intensity-based registration: a comparison and evaluation study. Phys Med Biol 59:4247–4260. doi:10.1088/0031-9155/59/15/4247
19. Murphy K, Van Ginneken B, Reinhardt JM, Kabus S, Ding K, Deng X, Cao K, Du K, Christensen GE, Garcia V, Vercauteren T, Ayache N, Commowick O, Malandain G, Glocker B, Paragios N, Navab N, Gorbunova V, Sporring J, De Bruijne M, Han X, Heinrich MP, Schnabel JA, Jenkinson M, Lorenz C, Modat M, McClelland JR, Ourselin S, Muenzing SEA, Viergever MA, De Nigris D, Collins DL, Arbel T, Peroni M, Li R, Sharp GC, Schmidt-Richberg A, Ehrhardt J, Werner R, Smeets D, Loeckx D, Song G, Tustison N, Avants B, Gee JC, Staring M, Klein S, Stoel BC, Urschler M, Werlberger M, Vandemeulebroucke J, Rit S, Sarrut D, Pluim JPW (2011) Evaluation of registration methods on thoracic CT: the EMPIRE10 challenge. IEEE Trans Med Imaging 30:1901–1920. doi:10.1109/TMI.2011.2158349
20. Weistrand O, Svensson S (2015) The ANACONDA algorithm for deformable image registration in radiotherapy. Med Phys 42:40–53. doi:10.1118/1.4894702
21. Sundaram TA, Gee JC (2005) Towards a model of lung biomechanics: pulmonary kinematics via registration of serial lung images. Med Image Anal 9:524–537. doi:10.1016/j.media.2005.04.002
22. Fuerst B, Mansi T, Carnis F, Sälzle M, Zhang J, Declerck J, Boettger T, Bayouth J, Navab N, Kamen A (2015) Patient-specific biomechanical model for the prediction of lung motion from 4-D CT images. IEEE Trans Med Imaging 34:599–607. doi:10.1109/TMI.2014.2363611
23. Werner R, Ehrhardt J, Schmidt R, Handels H (2009) Patient-specific finite element modeling of respiratory lung motion using 4D CT image data. Med Phys 36:1500–1511. doi:10.1118/1.3101820
24. Al-Mayah A, Moseley J, Velec M, Brock K (2008) Effect of friction and material compressibility on deformable modeling of human lung. Biomed Simul Int Symp 5104:98–106. doi:10.1007/978-3-540-70521-5_11
25. Li M, Castillo E, Zheng X-L, Luo H-Y, Castillo R, Wu Y, Guerrero T (2013) Modeling lung deformation: a combined deformable image registration method with spatially varying Young's modulus estimates. Med Phys 40:81902. doi:10.1118/1.4812419
26. Heinrich MP, Papiez BW, Schnabel JA, Handels H (2014) Non-parametric discrete registration with convex optimisation. Biomed Image Regist Springer Int Publ 8545:51–61. doi:10.1007/978-3-319-08554-8_6
27. Wang B, Tian X, Wang Q, Yang Y, Xie H, Zhang S, Gu L (2015) Pulmonary nodule detection in CT images based on shape constraint CV model. Med Phys 42:1241–1254. doi:10.1118/1.4907961
28. Glocker B, Komodakis N, Tziritas G, Navab N, Paragios N (2008) Dense image registration through MRFs and efficient linear programming. Med Image Anal 12:731–741. doi:10.1016/j.media.2008.03.006
29. James DL, Pai DK (1999) Accurate real time deformable objects. In: Proceedings of 26th annual conference on computer graphics and interactive techniques—SIGGRAPH '99, pp 65–72. doi:10.1145/311535.311542
30. Kim J, Choi C, De S, Srinivasan MA (2007) Virtual surgery simulation for medical training using multi-resolution organ models. Int J Med Robot Comput Assist Surg 3:149–158. doi:10.1002/rcs.140
31. Si H (2015) TetGen, a quality tetrahedral mesh generator. AMC Trans Math Softw 41:11. doi:10.1007/3-540-29090-7_9
32. Vandemeulebroucke J, Rit S, Kybic J, Clarysse P, Sarrut D (2011) Spatiotemporal motion estimation for respiratory-correlated imaging of the lungs. Med Phys 38:166–178. doi:10.1118/1.3523619
33. Murphy K, van Ginneken B, Klein S, Staring M, de Hoop BJ, Viergever MA, Pluim JPW (2011) Semi-automatic construction of reference standards for evaluation of image registration. Med Image Anal 15:71–84. doi:10.1016/j.media.2010.07.005
34. Heimann T, Van Ginneken B, Styner MA, Arzhaeva Y, Aurich V, Bauer C, Beck A, Becker C, Beichel R, Bekes G, Bello F, Binnig G, Bischof H, Bornik A, Cashman PMM, Chi Y, Córdova A, Dawant BM, Fidrich M, Furst JD, Furukawa D, Grenacher L, Hornegger J, Kainmüller D, Kitney RI, Kobatake H, Lamecker H, Lange T, Lee J, Lennon B, Li R, Li S, Meinzer HP, Németh G, Raicu DS, Rau AM, Van Rikxoort EM, Rousson M, Ruskó L, Saddi KA, Schmidt G, Seghers D, Shimizu A, Slagmolen P, Sorantin E, Soza G, Susomboon R, Waite JM, Wimmer A, Wolf I (2009) Comparison and evaluation of methods for liver segmentation from CT datasets. IEEE Trans Med Imaging 28:1251–1265. doi:10.1109/TMI.2009.2013851
35. Fortmeier D, Wilms M, Mastmeyer A, Handels H (2015) Direct visuo-haptic 4D volume rendering using respiratory motion models. IEEE Trans Haptics 8:371–383. doi:10.1109/TOH.2015.2445768